Bioactive Materials 37 (2024) 477–492

Contents lists available at ScienceDirect

Bioactive Materials

journal homepage: www.keaipublishing.com/en/journals/bioactive-materials

Durable immunomodulatory hierarchical patch for rotator cuff repairing

Liren Wang [a,d,1], Yonghang Liu [b,1], Zhiqi Lin [a,d], Huiang Chen [a,d], Bowen Liu [e], Xiaoyu Yan [a,d], Tonghe Zhu [b,**], Qin Zhang [c,***], Jinzhong Zhao [a,d,*]

[a] Department of Sports Medicine, Department of Orthopedics, Shanghai Institute of Microsurgery on Extremities, Shanghai Sixth People's Hospital Affiliated to Shanghai Jiao Tong University School of Medicine, No. 600 Yishan Road, Shanghai, 200233, China
[b] Multidisciplinary Centre for Advanced Materials, Institute for Frontier Medical Technology, School of Chemistry and Chemical Engineering, Shanghai University of Engineering Science, 333 Longteng Rd., Shanghai, 201620, China
[c] Institute of Translational Medicine, Shanghai University, 99 Shangda Rd., Shanghai, 200444, China
[d] Regenerative Sports Medicine and Translational Youth Science and Technology Innovation Workroom, Shanghai Jiao Tong University School of Medicine, No. 227 South Chongqing Road, Shanghai, 200025, China
[e] Bioarticure Medical Technology (Shanghai) Co., Ltd, Shanghai, China

ARTICLE INFO

Keywords:
Tendon-to-bone interface
Inflammation
Functional regeneration
Bioactive polymer
Bulk modification

ABSTRACT

Degradable rotator cuff patches, followed over five years, have been observed to exhibit high re-tear rates exceeding 50%, which is attributed to the inability of degradable polymers alone to restore the post-rotator cuff tear (RCT) inflammatory niche. Herein, poly(ester-ferulic acid-urethane)urea (PEFUU) was developed, featuring prolonged anti-inflammatory functionality, achieved by the integration of ferulic acid (FA) into the polyurethane repeating units. PEFUU stably releases FA in vitro, reversing the inflammatory niche produced by M1 macrophages and restoring the directed differentiation of stem cells. Utilizing PEFUU, hierarchical composite nanofiber patch (HCNP) was fabricated, simulating the natural microstructure of the tendon-to-bone interface with an aligned-random alignment. The incorporation of enzymatic hydrolysate derived from decellularized Wharton jelly tissue into the random layer could further enhance cartilage regeneration at the tendon-to-bone interface. Via rat RCT repairing model, HCNP possessing prolonged anti-inflammatory properties uniquely facilitated physiological healing at the tendon-to-bone interface's microstructure. The alignment of fibers was restored, and histologically, the characteristic tripartite distribution of collagen I – collagen II - collagen I was achieved. This study offers a universal approach to the functionalization of degradable polymers and provides a foundational reference for their future applications in promoting the in vivo regeneration of musculoskeletal tissues.

1. Introduction

The prevalence of rotator cuff tears (RCTs) exceeds 20% in the general population, making it a significant concern in shoulder joint pathologies [1]. Unlike the natural tendon-to-bone interface known for its mechanical integrity, surgical repair often results in scar tissue formation at the rotator cuff tendon and the humeral head interface [2,3]. This leads to a substantial reduction in mechanical performance, often less than 50% of the native strength, increasing the risk of postoperative retears [4,5].

The formation of scar tissue at the tendon-to-bone interface is closely associated with persistent inflammation at the residual cuff terminus [6,7]. Following an RCT, cell damage and structural degeneration within the tendon tissue initiate a prolonged inflammatory response [8]. This inflammation is sustained by mechanical stimuli from the remaining tendon tissue and eventually becomes chronic, disrupting the pro-regenerative niche for stem cells within the rotator cuff tissue [9,10]. If not addressed timely and effectively, this can lead to tissue necrosis or fibrosis, significantly impairing the natural regenerative capabilities of the rotator cuff tissue [11,12].

Peer review under responsibility of KeAi Communications Co., Ltd.
* Corresponding author. Shanghai Sixth People's Hospital Affiliated to Shanghai Jiao Tong University School of Medicine, No. 600 Yishan Road, Shanghai, China.
** Corresponding author.
*** Corresponding author.
E-mail addresses: zhutonghe89@sues.edu.cn (T. Zhu), sabrina_1985@shu.edu.cn (Q. Zhang), jzzhao@sjtu.edu.cn (J. Zhao).
[1] These authors contributed equally to this work.

https://doi.org/10.1016/j.bioactmat.2024.03.029
Received 24 December 2023; Received in revised form 29 February 2024; Accepted 25 March 2024

Currently, rotator cuff patches constructed from degradable polymers are being continuously optimized for the treatment of rotator cuff injuries. Proctor et al. found that among 18 patients with rotator cuff tears (RCT) who underwent reinforcement with poly-L-lactic acid (PLLA) patches, 15 showed intact continuity of the rotator cuff tissue in ultrasound examinations at 12 months postoperatively, with the American Shoulder and Elbow Surgeons (ASES) score improving from 25 to 71 ($P = 0.03$) within 12 months [13]. However, there was no statistical difference in ASES scores between patients who underwent repair with and without the PLLA patch at both 12 and 42 months postoperatively. Lenart et al. reported a high re-tear rate of 62% for rotator cuff repairs using PLLA patches two years after surgery [14]. The primary reason for this may be that the currently clinically used degradable rotator cuff patches are mainly composed of a single degradable polymer, which lacks sufficient regulatory effects on the pathological niche of tendon tissue after rotator cuff injury.

Current therapeutic strategies often involve incorporating anti-inflammatory small molecules into scaffolds, using various techniques such as coatings or blending [15,16]. However, these compounds typically have a short half-life of about one week and are prone to accelerated release kinetics in the dynamic in vivo environment [17–19]. This rapid release hinders the sustained establishment of an anti-inflammatory niche, thereby impeding tissue regeneration [20,21]. For example, Chen et al. used a hydrogel matrix for curcumin delivery in rat rotator cuff repair [22]. Their in vitro release assays revealed that over 70% of curcumin was released within the first week post-implantation, resulting in the regenerated rotator cuff tissue achieving only about 60% of the mechanical strength of normal tissue [23–25]. Recent advances in tissue engineering suggest that scaffolds designed to create an anti-inflammatory environment within the

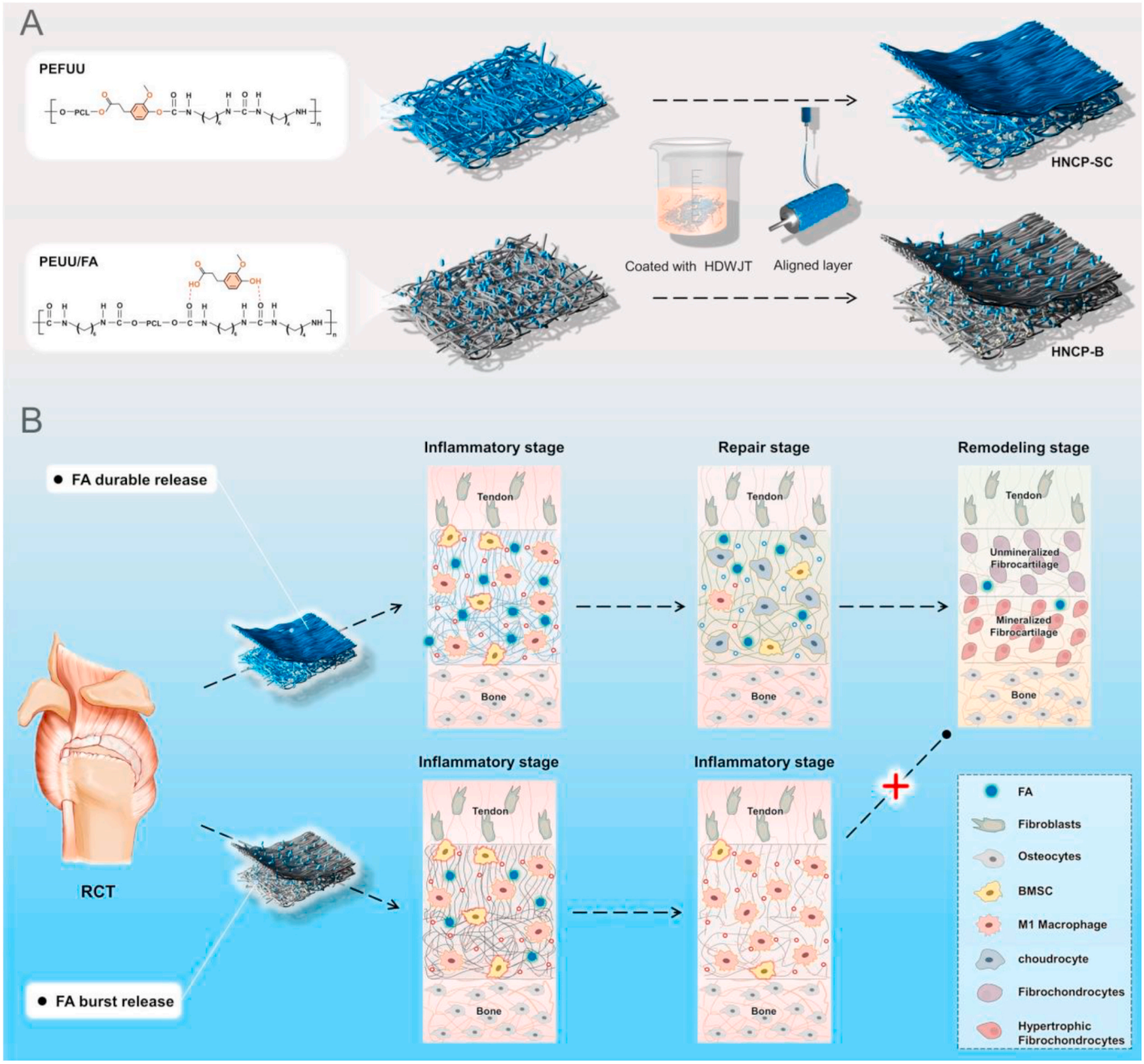

Scheme 1. Schemata of fabrication of the hierarchical composite nanofiber patch for rotator cuff tear repairing. (A) Fabrication of the hierarchical composite nanofiber patch via skeletal copolymerization (HNCP-SC) and hierarchical composite nanofiber patch via blending (HNCP–B); (B) HCNP-SC restores microstructural continuity at the tendon-to-bone interface by remodeling the niche post-injury.

regenerative niche could significantly improve the repair process of rotator cuff injuries [26]. These scaffolds aim to modulate the local tissue response, potentially enhancing healing outcomes and reducing degenerative changes [27–29].

Rossetti et al. observed that the extracellular matrix at the natural tendon-bone interface presents a structural gradient, with fibers transitioning from aligned at the tendon site to disordered at the bone site [30]. Replicating this microstructure could enhance the regeneration of the tendon-bone interface by closely mimicking autologous tissues. Aligned nanofibers support the expression of tendon-related genes in tendon cells, while randomly oriented nanofibers encourage chondrogenic gene expression in bone marrow mesenchymal stem cells [31]. Activating these genes is essential for the regenerative mechanism in rotator cuff repair. Thus, a bilayer nanofiber membrane with both aligned and random orientations could potentially improve rotator cuff repair and tendon-bone regeneration more effectively.

In this study, we developed a hierarchical composite nanofiber patch via skeletal copolymerization (HCNP-SC) with enduring immunomodulatory properties, capable of maintaining a prolonged anti-inflammatory microenvironment conducive to tissue regeneration (Scheme 1). We synthesized a degradable poly(ester-ferulic acid-urethane)urea (PEFUU) with ferulic acid (FA) as a bioactive component. PEFUU was then electrospun to create a bipolar fiber patch with an organized, yet partially random, stratified architecture. The random layer of this architecture was infused with the enzymatic hydrolysate from decellularized Wharton jelly tissue (HDWJT). In vitro experiments showed a gradual release of FA, coinciding with the progressive degradation of the HCNP-SC. In an in vivo rat model of tendon-to-bone injury, the HCNP restored microstructural continuity at the tendon-bone interface and established a trinomial distribution of collagen ordering. These findings support the HCNP-SC as a multifunctional platform with the potential to facilitate reparative processes at heterogeneous interfaces within the musculoskeletal system.

2. Experimental section/methods

2.1. Study design

The aim of this study was to develop a hierarchical patch with sustained immunomodulatory effects for rotator cuff (RC) repair. Initially, we incorporated ferulic acid (FA) into the repeating units of a degradable polyurethane polymer through backbone copolymerization. Following successful synthesis confirmation via nuclear magnetic resonance (NMR), we rigorously assessed the anti-inflammatory properties of the resulting poly(ester-ferulic acid-urethane)urea (PEFUU). In particular, we evaluated the prolonged anti-inflammatory effects by conducting repeated inflammation assays to mimic the interaction between patch degradation fluid and bodily fluids in vivo. Additionally, using protein arrays, we demonstrated that PEFUU degradation fluid can prompt macrophages to release anti-inflammatory factors in an in vitro inflammatory setting. We also confirmed the protective influence of PEFUU degradation fluid on the directed differentiation of stem cells in an inflammatory environment. To improve the recruitment and directed differentiation of stem cells on the degradable polyurethane surface, we incorporated the enzymatic hydrolysate from decellularized Wharton jelly tissue (HDWJT) into the random layer of the hierarchical electrospun patch after freeze-drying and validated the mechanical properties of the composite patch.

To evaluate the reparative efficacy of the composite patch in vivo, we employed the patch in a rat model (250 g) for RC injury repair. The animals were allocated into four groups: (1) RC defect group; (2) simple surgical repair group; (3) HCNP via blending repair group; and (4) HCNP via backbone copolymerization repair group. Observations and sampling were conducted at 1 and 2 months post-surgery for each group. Following the guidelines for experimental animal study design, we selected 6 rats for each group. At each sampling time point, the rats were euthanized via overdose anesthesia, and subsequent radiological, histological, biomechanical, and molecular biological analyses were conducted.

2.2. Synthesis of PEFUU

The dynamic simulation of PEFUU was performed using Material Studio 8.0 software. The poly(ester-ferulic acid-urethane)urea (PEFUU) was synthesized as follows: poly(Ɛ-caprolactone) (PCL) and FA were accurately weighed (molar ratio of 1:0.15) and transferred to a three-neck flask under a nitrogen atmosphere. The reaction proceeded at 120 °C for 8 h, with the water generated during the reaction being removed via vacuum treatment. Subsequently, the reaction temperature was lowered to 80 °C, and hexamethylene diisocyanate (HDI) was added for a 2-h pre-polymerization reaction. The reaction temperature was then further reduced to 40 °C, and chain extension was carried out by adding 1,4-diaminobutane (DAB) for 18 h. The molar ratio of PCL, HDI, and DAB was maintained at 1:2:1. Upon completion of the reaction, the product was purified using deionized water for 3 days, followed by freeze-drying to obtain the pure PEFUU elastomer. The yield of PEFUU was calculated to be as high as 90%. The chemical structure of PEFUU was evaluated using ^{1}H NMR spectroscopy, with deuterated dimethyl sulfoxide (DMSO) as the solvent.

2.3. Preparation of HCNP -SC

HCNP-SC was fabricated using the following procedure. Initially, PEFUU was dissolved in 1,1,1,3,3,3-hexafluoro-2-propanol to create a 10% solution. This solution was then stirred overnight using a magnetic stirrer to ensure uniformity. The electrospinning technique was employed to produce the fiber layer. Specifically, the clear solution was drawn into a 50 mL syringe and positioned approximately 12 cm away from aluminum foil. The solution was then dispensed at a rate of 0.10 mL/h under a voltage of +1 kV, with the drum rotating at 50 rpm at room temperature (25 °C). After completing the spinning process, the aluminum foil and the electrospun scaffold (random layer) were collected for further experimentation. Decellularized Wharton jelly was obtained from Bioarticure Medical Technology (Shanghai) Co., Ltd. For enzymatic hydrolysis, a papain-PBS solution (pH 6.5) containing 125 μg/mL papain, 5 mM ethylenediaminetetraacetic acid (EDTA), and 5 mM cysteine was prepared. We then treated 100 mg of decellularized Wharton jelly with 10 ml of this solution and allowed it to react overnight at 60 °C. The aluminum foil and its electrospun scaffold (random layer) were placed in a Petri dish and lyophilized along with the hydrolyzed Wharton jelly. The dish was then frozen at −80 °C, and the samples were freeze-dried to remove water. After freeze-drying, the aluminum foil with the enzyme-hydrolyzed decellularized Wharton jelly was placed back on the electrospinning drum, which was set to rotate at 2500 rpm. The electrospinning process was then initiated to prepare the orientation layer. Finally, after completing the aligned layer (oriented towards the tendon's remnant end), the HCNP-SC was collected for subsequent use.

2.4. Drug release

To verify the sustained release of PEFUU, 5 mg PEFUU and 5 mg PEUU/FA polymer were immersed in centrifuge tubes containing 5 mL of phosphate-buffered saline (PBS). Samples were collected at predetermined time intervals. The content of FA in the degradation solution was calculated using a high-performance liquid chromatography system (ALLIANCE e2695, Waters Corporation, USA), and the cumulative release rate (R) of ferulic acid was calculated using the following formula:

$$R\ (\%) = \frac{m_e}{m_0} \times 100\% \quad (1)$$

where m_0 is the mass of FA present in the fibers and me is the amount of FA released at a specific time point.

The relative release rate (V) of FA was calculated as follows:

$$V = \frac{R_n - R_{n-1}}{T_n - T_{n-1}} \quad (2)$$

where R is the cumulative release rate of FA at a specific time, and T is the total degradation time.

2.5. In vitro evaluation of the antioxidant activity of degradation fluid

The antioxidant activity of the degradation fluid was verified using the DPPH scavenging assay. First, 100 μg of DPPH was dissolved in 10 mL ethanol. Next, 80 μL of the DPPH solution was removed and added to a 96-well plate, followed by 20 μL of degradation fluid obtained at a specific time point. Further, 80 μL DPPH solution mixed with 20 μL of PBS was used as a control. After incubation in the dark for 10 min, the optical density (OD) value was measured at 517 nm using a microplate reader. The antioxidant efficiency (Ls) of the sample was calculated using the following formula:

$$L_s\ (\%) = \frac{OD_c - OD_s}{OD_s} \times 100\% \quad (3)$$

where ODc and ODs represent the OD values of the control and experimental groups, respectively.

2.6. Repeated evaluation of antioxidant capacity

First, 5 mg PEFUU and PEUU/FA polymer were placed in 5 mL of PBS for 3 days. After 3 days, the antioxidant activity of the degradation fluid was tested as previously described. This value was recorded as the first antioxidant efficiency. Then, PEFUU and PEUU/FA polymers were removed from the degradation liquid and placed in 5 mL of fresh PBS for 3 days. After 3 days, the antioxidant activity of the degradation fluid was tested again. This value was recorded as the second antioxidant efficiency. This process was repeated up to eight times.

2.7. Macrophage polarization

PEFUU (100 mg) was mixed with 10 mL of high-glucose Dulbecco's Modified Eagle Medium (DMEM) and incubated in a 37 °C, 0.5% CO2 incubator for 7 days. Subsequently, PEFUU degradation fluid was collected and stored in a 4 °C refrigerator for later use. The effect of PEFUU on macrophage polarization was evaluated using mouse mononuclear macrophages (RAW 264.7). Fetal bovine serum, antibiotics, and other induction factors (M1 macrophage-inducing factor: LPS, 100 ng/mL; M2 macrophage-inducing factors: IL-4 20 ng/mL + IL-13 20 ng/mL) were added to simple DMEM (M1 group or M2 group) and experimental PEFUU degradation fluid (M1 + PEFUU group or M2 + PEFUU group) to prepare different culture media. Complete DMEM without induction factors (LPS or IL-4 + IL-13) was used as a negative control (M0 group). RAW 264.7 cells from each group were cultured with their corresponding medium for 48 h and collected for further experiments.

2.8. Immunofluorescence staining of macrophages

For each group of cells, the medium was removed, and the cells were washed thrice with PBS. After that, the cells were fixed with 0.5% glutaraldehyde solution for 30 min. Then, the cells were incubated with 1.5% Triton X-100 solution (for 30 min), 5% bovine serum albumin (for 30 min), and primary antibodies against iNOS or CD206 (overnight at 4 °C). The following day, the cells were washed thrice with PBS and incubated with secondary antibodies for 2 h. The cells were finally stained with rhodamine-labeled phalloidin (30 min), followed by DAPI (15 min), and observed under a fluorescence microscope.

2.9. ROS detection

After culture, cells from the M0, M1, and M1 + PEFUU groups were stained with DCFH-DA, which was diluted with DMEM (w:w = 1:1000), and incubated for 20 min in a CO2 cell culture incubator. Subsequently, images were recorded using a fluorescence microscope (DMi8; Leica).

2.10. Effect of PEFUU degradation fluid on inflammatory factors and gene expression in polarized macrophages

Culture medium from the M0, M1, and M1 + PEFUU groups was collected and tested using a Mouse Inflammation Array Q1 according to instructions from the manufacturer. The cells from the M0, M1, M2, M1+ PEFUU, and M2 + PEFUU groups were collected, and their RNA was extracted. After reverse transcription, inflammation-related gene expression was evaluated using RT-qPCR according to the manufacturer's instructions. The primer sequences are presented in Table S1.

2.11. Protective effect of PEFUU degradation fluid on BMSCs

Culture medium from the M1 and M1 + PEFUU groups was collected and mixed with chondrogenic induction factors. Each medium mixture was used for the chondrogenic differentiation of BMSCs. After 14 days of culture, the protective effect of PEFUU degradation fluid was evaluated based on immunofluorescence staining for Sox9.

2.12. Protective effect of the PEFUU degradation fluid on tendon-derived stem cells (TDSCs)

Culture medium from the M1 and M1 + PEFUU groups was collected and used for TDSC culture. After 6 days of culture, the protective effect of PEFUU degradation fluid was evaluated based on immunofluorescence staining for Scx.

2.13. Preparation of HDWJT

DWJ tissue was obtained from Bioarticure Medical Technology (Shanghai) Co., Ltd. First, the papain solution was prepared (papain 125 μg/mL, 5 mM EDTA, 5 mM cysteine) at pH = 6.5. Subsequently, 100 mg of DWJ was immersed in 10 mL of the papain solution at 60 °C overnight. The clear solution was frozen at −80 °C and lyophilized to obtain the HDWJT powder. HDWJT powder was dissolved in complete αMEM to prepare the WJ complete medium. BMSCs were divided into two groups and cultured in 6-well plates using either pure complete αMEM or WJ complete medium. After 7 days of culture, the cells were collected using TRIzol (Vazyme, R401-01-AA) and sent to Meiji Biology for further experiments and analysis.

2.14. Effect of HDWJT on BMSC chondrogenesis

HDWJT powder was dissolved in chondrogenic induction medium to prepare the WJ chondrogenic induction medium. BMSCs were divided into two groups in a 24-well plate: one group was cultured with simple chondrogenic induction medium, while the other was cultured with WJ chondrogenic induction medium. After 14 days of culture, immunofluorescence staining for collagen II and aggrecan and RT-qPCR were conducted to evaluate the chondrogenic capacity of BMSCs in each group.

2.15. Characterization of the HCNP-SC

The surface morphology of the HCNP was evaluated using SEM and materials confocal microscopy. The mechanical property of the HCNP was examined using Instron.

2.16. Establishment of a tendon-to-bone interface tear

Male Sprague–Dawley rats (approximately 250 g) were obtained from the Shanghai Sixth People's Hospital Affiliated to Shanghai Jiao Tong University School of Medicine. All procedures involving animal use, care, and handling were conducted under the supervision of the Animal Welfare and Ethics Committee of the Shanghai Sixth People's Hospital Affiliated to Shanghai Jiao Tong University School of Medicine (approval number 20150119-013).

The rats were randomly divided into four groups: defect group, simple surgical repair (SR) group, HCNP via blending (HCNP–B) group, and HCNP via skeletal copolymerization (HCNP-SC) group. After anesthesia, the shoulders of the rats were shaved and sterilized. After palpating the greater tubercle of the humeral head, a 1.5 cm incision was made centered on the tubercle. The subcutaneous fascia and the deltoid muscle layer were sequentially exposed in layers until the rotator cuff tissue was visualized. The supraspinatus tendon was surgically cut at its footprint area on humeral head using a No. 10 blade. The residual cartilage tissue in the footprint area of the RC humeral head was also perturbed. In the defect group, the deltoid muscle and skin tissue were sutured one after the other, without repairing the RC tendon defect. In the SR group, two bone tunnels were first established on the humeral head (diameter of 0.6 mm in the footprint area of the RC). Then, using No. 4 non-absorbable nylon sutures, the residual RC tissue was fixed to its footprint area on the humeral head by crisscrossing through the two bone tunnels. In the HCNP–B group, the patch was added between the residual tendon tissue and the footprint area of the humeral head. In the HCNP-SC group, patch was added between the residual tendon tissue and the footprint area of the humeral head. Within 3 days post-surgery, each rat received penicillin injections to prevent infection. There was no activity restriction for the rats postoperatively. At 1 and 2 months post-surgery, the rats were euthanized via an overdose of 3% pentobarbital sodium. The rat RC–humeral complex was harvested and fixed for subsequent analysis.

2.17. Evaluation of the tendon-to-bone interface and tendon regeneration

Fixed rat RC-humeral complex specimens were placed in decalcifying fluid for 1 month until they were suitable for sectioning. After dehydration, embedding, sectioning (5 μm), and staining with SO/Fast Green, the tendon-to-bone interface was observed under a light microscope. For XRM, after fixation using 4% polyformaldehyde, the RC–humeral complex was immersed in Lugol's iodine solution for 48 h. Subsequently, the complex was transferred to 70% ethanol for 12 h and stored in 100% ethanol. Then, the 3-dimensional microstructure of the tendon-to-bone interface was observed using a Zeiss 520 Versa microscope, with exposure for 3 s at 7 W and 80 kV. Dragonfly (Object Research Systems, Canada) was used for remodeling. For SEM evaluation, after frozen sectioning, the sections were observed using RISE-MAGNA (TESCAN, Czech Republic). For immunofluorescence staining, sections were stained with the corresponding antibody and observed under an inverted fluorescence microscope. After the harvest of the rat RC–humeral complex, 1 mm3 tendon tissue was collected and fixed using 2.5% glutaraldehyde. After dehydration and embedding in resin, the tissue was cut into thin slices (5 μm) and observed using a Tecnai G2 microscope (Thermofisher, USA).

2.18. Statistical analysis

One-way ANOVA were used for statistical analysis of experimental data. Graphical analysis was performed using Prism Graph 9 and Origin Pro (Student Version). Transcriptional analysis graphs were created using free online platforms for data analysis and visualization (https://www.omicstudio.cn, and https://www.xiantao.love). All data will be presented as mean ± standard deviation (Mean ± SD). Results with $P < 0.05$ (*) will be considered as statistical significance.

3. Results

3.1. Synthesis of PEFUU and evaluation of its antioxidant ability

To synthesize the anti-inflammatory polymer PEFUU, PCL was functionalized with FA, followed by pre-polymerization and chain extension using HDI and DAB, respectively (Fig. S1). Prior to synthesizing PEFUU, its kinetics were analyzed (Fig. 1A and B), demonstrating good spatial extensibility of the repeating units, which confirms the feasibility of the synthesis strategy. The ^{1}H NMR spectra of PEFUU and FA are presented in Fig. 1C. The characteristic absorption peaks of the phenyl ring segment are evident in the 6.8–7.3 ppm region for FA and around the 7-ppm region for PEFUU, indicating successful incorporation of FA into the polyurethane backbone. The FA release behavior from PEFUU is illustrated in Fig. 1D–G. As PEFUU degraded, FA fragments were released, enabling sustained drug release. On the first day, PEUU/FA fibers, prepared through simple blending, released 59.37 ± 2.87% of FA, which stabilized at 64.47 ± 4.34% after 48 h. In contrast, PEFUU exhibited a more controlled release, with only 7.13 ± 0.06% of FA released after 24 days, as shown in Fig. 1D. The initial release rate of FA from PEUU/FA was high at 105.14 ± 14.98 μg/day during the first 6 h but decreased sharply to 5.73 ± 16.01 μg/day at 36 h, indicating a burst release pattern. On the other hand, PEFUU maintained a stable FA release rate of approximately 0.2 μg/day from 0 to 24 days, suggesting a more effective and consistent FA release over this period, as depicted in Fig. 1E.

The antioxidant efficiency of the degradation solutions was assessed using a DPPH scavenging assay, as shown in Fig. 1F. Although the antioxidant efficiency of both PEFUU and PEUU/FA degradation solutions increased over time, the correlation between FA release and antioxidant activity was more linear for the PEFUU degradation solution. Furthermore, the FA content in the PEUU/FA degradation solution did not significantly increase beyond 35.04%, indicating a potential over-release of FA in the early stages. The relative antioxidative rates of PEUU/FA and PEFUU (Fig. 1G) revealed that the antioxidative rate of PEUU/FA was lower, likely due to the excessive initial release of FA, resulting in a reduced release in later stages. In contrast, the antioxidative rate of PEFUU progressively increased, possibly due to the polymer's gradual degradation, leading to a continuous release of FA, especially in the later stages compared to the initial phase. To mimic the anti-inflammatory infiltration ability of polymers under dynamic body fluid exchange conditions in vivo, the degradation solutions of PEFUU and PEUU/FA for DPPH scavenging experiments were repeatedly obtained (Fig. 1H). The antioxidant activity of the PEUU/FA degradation solution rapidly decreased from 84.95 ± 0.23% in the first round to 10.14 ± 0.28% in the third round. In contrast, the antioxidant activity of PEFUU remained stable, ranging between 40.28% and 42.09% across the first to eighth rounds of degradation. This difference in the area under the curve between the two polymers (Fig. 1I–K) suggested that PEFUU fibers, capable of slow and persistent FA release, may promote better FA antioxidant activity, as illustrated in Fig. 1L.

3.2. Remodeling the inflammatory niche from PEFUU

To investigate the regulatory effects of PEFUU degradation products on macrophages during inflammation, we compared the influence of PEFUU degradation fluid on the polarization of M1 and M2 macrophages, as shown in Fig. 2A. The results, depicted in Fig. 2B, showed a significant increase in the percentage of CD206-positive macrophages in the M2 macrophage control group (induced by IL-4 + IL-13) to 43.04 ± 4.45%, compared to the normal control group (0.84 ± 0.31%) (Fig. S2). The addition of PEFUU degradation fluid to the M2 macrophage induction solution further elevated the proportion of CD206-positive macrophages to 85.04 ± 3.31%. In the M1 macrophage control group, induced by LPS + IFN-α, the proportion of iNOS-positive macrophages was markedly higher at 91.30 ± 2.31% than in the normal control group

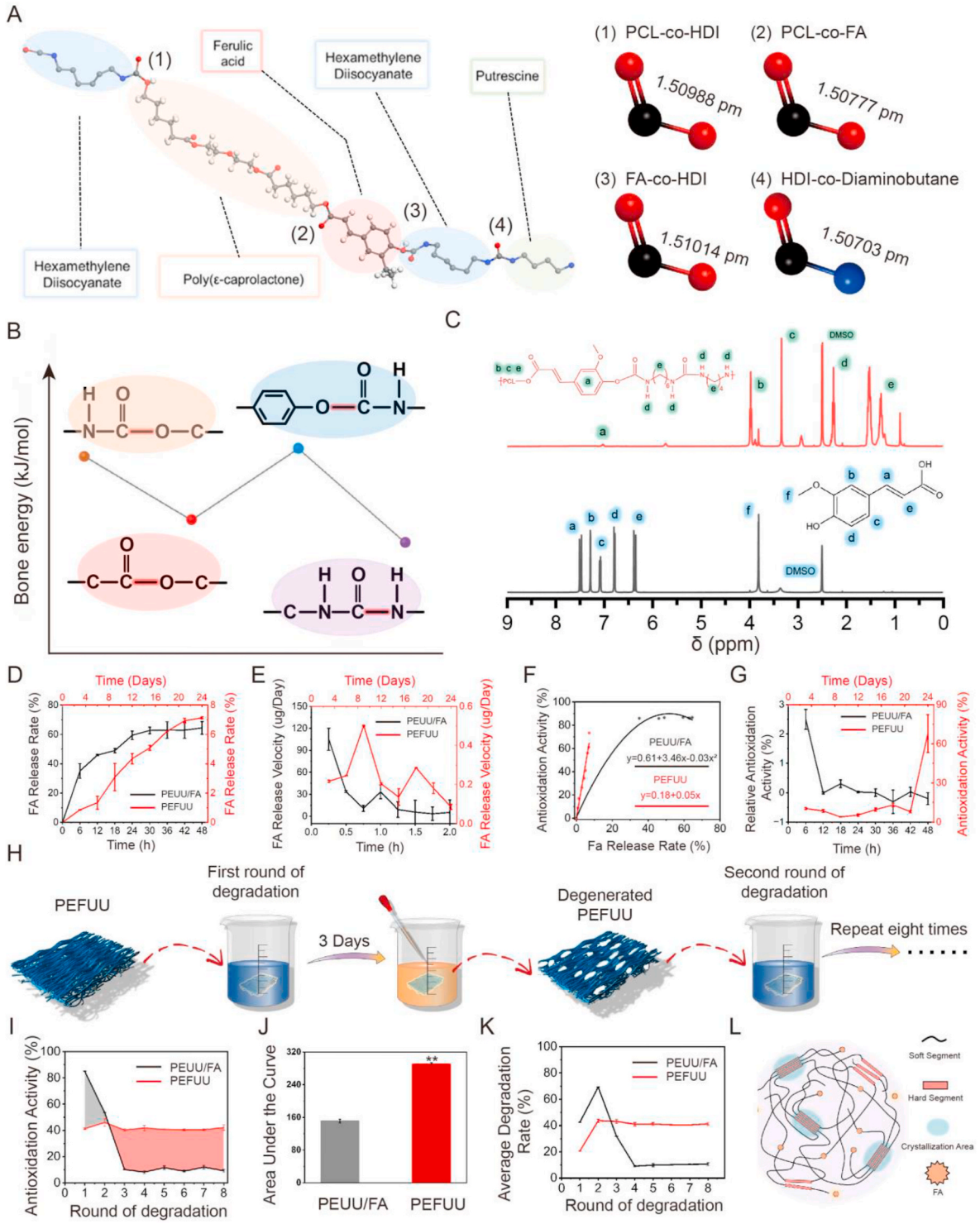

Fig. 1. Synthesis and antioxidant evaluation of PEFUU. (A–B) Schematic image showing the molecular dynamics simulation of PEFUU. (C) Local ^{1}H nuclear magnetic resonance spectrum of PEFUU (red curve) and FA (black curve). (D–G) Release speed of ferulic acid and its antioxidation activity from the anti-inflammatory polymer and PEUU/ferulic acid blend polymer (n = 3). (H) Repeated anti-inflammatory function testing of the PEFUU and PEUU/FA polymer; (I - K) Relationship between DPPH scavenging efficiency and the round of degradation in PEFUU and PEUU/FA polymers (n = 3). (L) Schematic image of ferulic acid release from PEFUU.

(1.34 ± 1.57%) (Fig. S3). The inclusion of PEFUU degradation fluid during M1 macrophage induction significantly reduced iNOS-positive macrophages to 37.37 ± 10.38%. Flow cytometry results, as presented in Fig. S4, further supported these findings. After polarization induction with LPS and IL-4 + IL-13, the proportion of iNOS + CD206- (M1)/iNOS-CD206+ (M2) mouse macrophages was 47.8% and 8.73%, respectively. Treatment with PEFUU degradation fluid decreased the proportion of M1 macrophages to 34.3%, while increasing the proportion of M2 macrophages to 17.34%. Additionally, the expression levels of reactive oxygen species (ROS) in untreated and PEFUU degradation fluid-treated M1 macrophages were compared, as shown in Fig. S5. The PEFUU degradation fluid significantly reduced ROS levels in macrophages from 75.98 ± 10.24% to 13.93 ± 3.79%, suggesting a mechanism by which PEFUU degradation fluid inhibits polarization towards the M1 state and

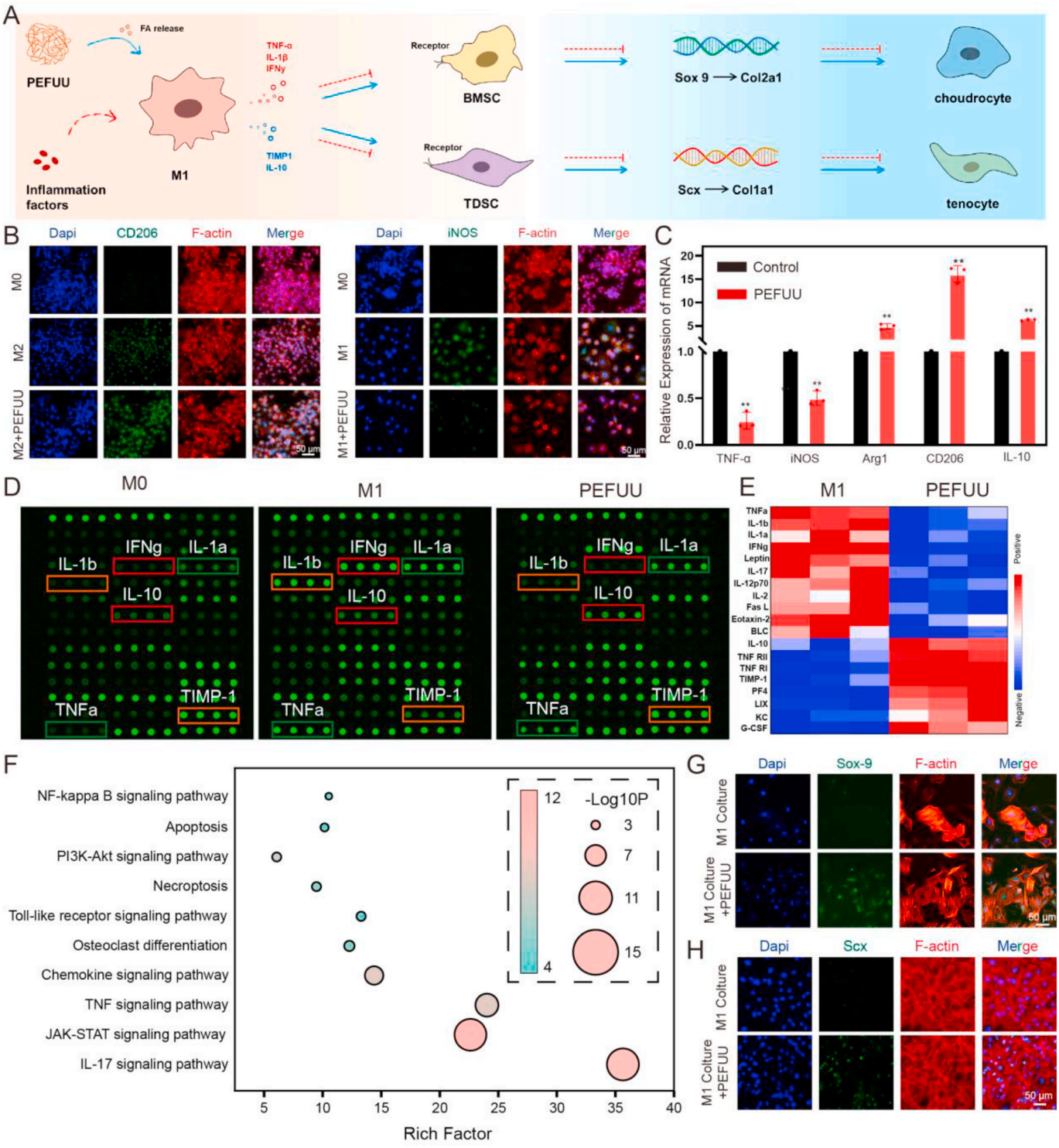

Fig. 2. PEFUU provides a pro-regenerative niche by modulating macrophage polarization. (A) Schemata of FA released from PEFUU to modulate macrophage polarization for providing a pro-regenerative niche; (B) Representative images of immunofluorescent staining of iNOS and CD206 in macrophages under different induction conditions; (C) RT-qPCR-based analysis of the effects of PEFUU degradation products on macrophage polarization; (D) Protein chip detection and (E) the heat map of inflammation-related protein secretion in macrophages under different induction conditions; (F) KEGG pathway analysis of differential protein between M1 induction group and M1 induction + PEFUU degradation products group; (G) Immunofluorescence staining for Sox9 (green)and F-Actin (red) as chondrogenic markers in bone marrow mesenchymal stem cells cultured with different supernatants; (H) Immunofluorescence staining for Scx (green)and F-Actin (red) as tenogenic markers in tendon stem cells cultured with different supernatants. **, $P < 0.01$ compared with the defect group, indicating a significant difference.

promotes polarization towards the M2 state. PCR results, displayed in Fig. 2C, revealed that PEFUU degradation fluid can enhance the expression of M2-related genes while suppressing M1-related genes. The secretion of inflammation-associated proteins by M1 macrophages, both with and without PEFUU degradation solution treatment, was compared in Fig. 2D and E. Under standard M1 induction, macrophages secreted a significant amount of pro-inflammatory proteins (e.g., TNFα, IL-1β). However, the addition of PEFUU degradation solution led to a marked

decrease in the secretion of these pro-inflammatory proteins, with a concurrent increase in proteins conducive to tissue regeneration (e.g., IL-10, TIMP-1), indicating a shift from an inflammatory to a pro-repair niche. KEGG pathway analysis, as shown in Fig. 2F, indicated that PEFUU degradation solution primarily modifies the inflammatory pathway.

To assess the impact of different polarization states on stem cell differentiation under inflammatory conditions, supernatants of M1 macrophages were used to induce chondrogenic and osteogenic differentiation in rat bone marrow mesenchymal stem cells (BMSCs) and tendon differentiation in rat tendon derived stem cells (TDSC), as depicted in Fig. 2G and H. In chondrogenic differentiation experiments (Figs. S6 and S7), BMSCs treated with M1 macrophage supernatant + PEFUU degradation solution exhibited a significantly higher proportion of SOX9-positive cells (56.46 ± 4.69%) compared to those treated with only M1 macrophage supernatant (13.46 ± 4.15%). Additionally, pellets cultured in M1 macrophage supernatant + PEFUU degradation solution showed deeper Alcian blue staining and higher collagen II presence, indicating enhanced chondrogenic differentiation, compared to those treated with only M1 macrophage supernatant. In osteogenic differentiation experiments (see Supplementary Fig. S8), BMSCs treated with M1 macrophage supernatant + PEFUU degradation solution displayed more pronounced Alizarin Red S and Alkaline Phosphatase (ALP) staining, indicative of increased intracellular mineralization and ALP activity, suggesting stronger osteogenic differentiation capability. Furthermore, the capacity of TDSC to produce tendon collagen in media containing M1 macrophage supernatant, with or without PEFUU degradation solution, was compared. A greater proportion of SCX-positive TDSC (37.97 ± 4.75%) and higher relative fluorescence intensity of collagen I were observed in the group treated with M1 macrophage supernatant + PEFUU degradation solution compared to the group treated with only M1 macrophage supernatant (8.96 ± 4.93%), as shown in Figs. S9 and S10. These findings from stem cell-induced differentiation experiments suggest that the degradation products of PEFUU can facilitate the restoration of directed differentiation capabilities of stem cells in an inflammatory environment, thereby laying the groundwork for physiologically relevant tissue regeneration.

3.3. Validation of the pro-regenerative effects of HDWJT and construction of the HCNP

RNA sequencing was performed on bone marrow mesenchymal stem cells (BMSCs) cultured in control and Wharton's Jelly (WJ) media. Our study revealed a significant change in gene expression: 220 genes were upregulated and 17 genes were downregulated in cells cultured in WJ media, as depicted in Fig. 3A. KEGG pathway analysis identified notably upregulated pathways, including extracellular matrix (ECM) receptor interaction, Wnt signaling pathway, and focal adhesion (Fig. 3B). Genes important for modulating the interaction between stem cells and patches, such as Col9a1 and Col4a4, showed upregulation in response to increased HDWJT concentrations, suggesting that HDWJT treatment effectively enhances stem cells' responsiveness to the patch (Fig. 3C). Immunofluorescence staining further confirmed the impact of DWJ on chondrogenic differentiation (Fig. 3D and E). After DWJ treatment, the proportion of collagen II- (61.06 ± 8.41%) and aggrecan-positive cells (65.19 ± 2.16%) in the experimental group was significantly higher than that in the control group (40.65 ± 4.60% and 53.14 ± 4.26%, respectively), as shown in Figs. S11 and S12. Real-time quantitative PCR (RT-qPCR) was used to validate the upregulation of these pathways and their association with chondrogenic gene expression. A significant increase in the expression of chondrogenic markers, including Sox9 and collagen II, was observed in these cells (Fig. S13), indicating that DWJ notably enhances BMSCs' responsiveness to random patch structures and promotes their chondrogenic differentiation. These in vitro findings provide a solid foundation for promoting the regeneration of tendon–bone interfaces in vivo.

Following the elucidation of the biological effects of PEFUU and HDWJT, an HCNP-SC was fabricated using electrospinning (Fig. 3F). The aligned layer of the HCNP consisted of oriented, smooth, and uniform fibers (Fig. 3G). Meanwhile, the random layer was infused with HDWJT using a freeze-drying method, resulting in protein-like protrusions on the surface of the patch. A comparison of the mechanical properties of our HCNP with those reported in 10 other studies was conducted (Fig. 3H). The tensile strength of our HCNP was 54.95 ± 13.81 MPa, with a maximum elongation of 98.36 ± 11.21% (Fig. S14). Compared to other degradable polyurethanes used in tissue engineering, our HCNP demonstrated superior tensile strength, which could prevent tearing due to excessive mechanical stress post-implantation. Results from live/dead staining and CCK-8 assays suggest that cell proliferation on HCNP-SC is comparable to the control group cultured in flat dishes (Fig. S15). Therefore, the potential of this bionic bipolar patch in the repair of musculoskeletal injuries warrants further exploration.

3.4. HCNP-SC promotes the microstructural healing of the tendon-to-bone interface

The regeneration of tissue following RCT requires the precise establishment of a suitable regenerative niche (Fig. 4A). HCNP–B, based on PEUU/FA, and HCNP-SC, constructed from PEFUU, were used for rotator cuff repair in rats, with defect and surgical repairing (SR) groups serving as controls. One month post-surgery, it was noted that the tendons in the defect group had not healed, and the repaired rotator cuff tissue in the SR group appeared thinner (Fig. 4B). An increase in synovial tissue was observed in the HCNP–B group, likely due to an inflammatory response triggered by polymer degradation. In the HCNP-SC group, the regenerated tissue had not yet fully transformed into tendon tissue. CT results at 10 μm resolution revealed that the bone mineral density (BMD) and bone volume to total volume (BV/TV) (Fig. 4C and D) of subcortical bone in the rotator cuff footprint area of the SR, HCNP–B, and HCNP-SC groups were higher compared to the defect group. One month post-surgery, the bone mineral density (BMD) and bone volume to total volume (BV/TV) were higher in the SR group (BMD: 0.40 ± 0.02 g/cm^2; BV/TV: 39.07 ± 3.49%), HCNP–B group (BMD: 0.47 ± 0.01 g/cm^2; BV/TV: 42.24 ± 3.17%), and HCNP-SC group (BMD: 0.51 ± 0.01 g/cm^2; BV/TV: 47.99 ± 2.28%) compared to the defect group (BMD: 0.32 ± 0.03 g/cm^2; BV/TV: 34.34 ± 4.55%). At 1 μm resolution, no tendon tissue connected to cortical bone was observed in the defect group's rotator cuff footprint area. Thin fibrous tissue connections to cortical bone were visible in the SR and HCNP–B groups. A robust connection between tendon tissue and cortical bone was noted in the HCNP-SC group. At 0.1 μm resolution, no fibrous connections on cortical bone were seen in the defect group. While tendon fibers were present in the SR group, they did not form healing connections with cortical bone. Tendon fibers in the HCNP–B group were healed to cortical bone, but their arrangement was discontinuous. In the HCNP-SC group, a healed tendon-bone interface with a microscopic structure was observed. The microscopic structural histological score (Fig. 4E) in the defect group was significantly lower (6.33 ± 0.52) than in the SR (13.17 ± 0.75), HCNP–B (11.33 ± 0.82), and HCNP-SC groups (13.33 ± 0.52).

Two months post-surgery, tissue defects in the rotator cuff tissue were noted in the defect group upon gross observation. The rotator cuff tendon in the SR group was noticeably thinner. Further proliferation of synovial tissue on the rotator cuff tissue was seen in the HCNP–B group, indicating long-term inflammatory infiltration due to the HCNP–B scaffold. Physiological regeneration of rotator cuff tissue was evident in the HCNP-SC group, suggesting the promotion of tissue regeneration after rotator cuff repair by HCNP-SC. Two months post-surgery, the HCNP-SC group (BMD: 0.57 ± 0.01 g/cm^2; BV/TV: 57.38 ± 2.97%) exhibited the highest bone density and volume, followed by the HCNP–B group (BMD: 0.51 ± 0.01 g/cm^2; BV/TV: 48.23 ± 3.74%), and the SR group (BMD: 0.44 ± 0.02 g/cm^2; BV/TV: 44.46 ± 2.65%), compared to the defect group (BMD: 0.39 ± 0.02 g/cm^2; BV/TV: 37.97 ± 2.51%). At

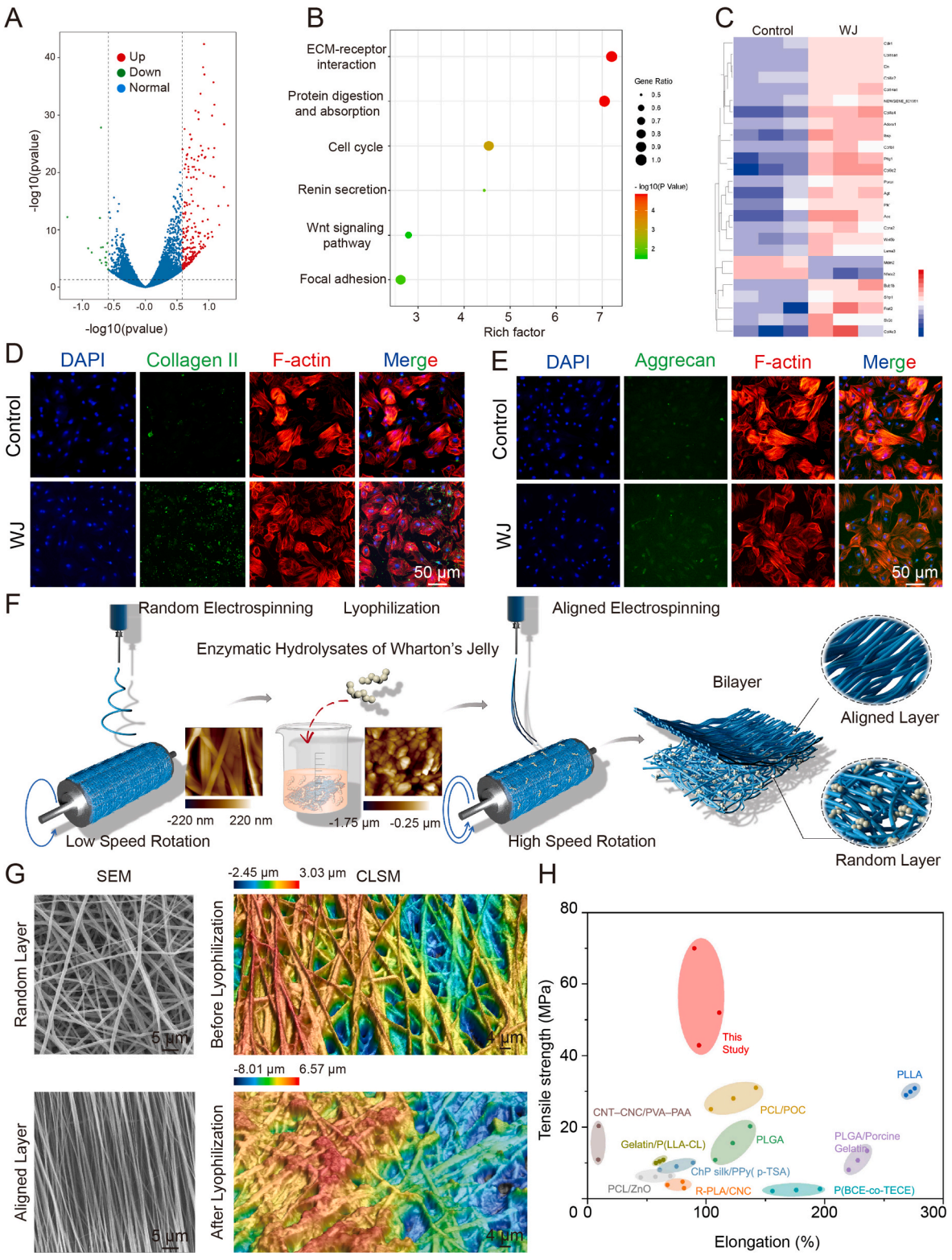

Fig. 3. Validation of HDWJT's biological effects and HCNP construction: (A) Volcano plot comparing gene expression in rat BMSCs co-cultured with HDWJT versus untreated BMSCs; (B) KEGG pathway analysis of significant differentially expressed genes; (C) Heatmap of key differentially expressed genes (red for upregulated, blue for downregulated) in control cells versus cells co-cultured with HDWJT; Immunofluorescence staining for (D) collagen II and (E) aggrecan in untreated and HDWJT co-cultured rat BMSCs post-chondrogenic induction; (F) HCNP construction; (G) HCNP surface morphology; (H) Mechanical property comparison of HCNP from previous studies.

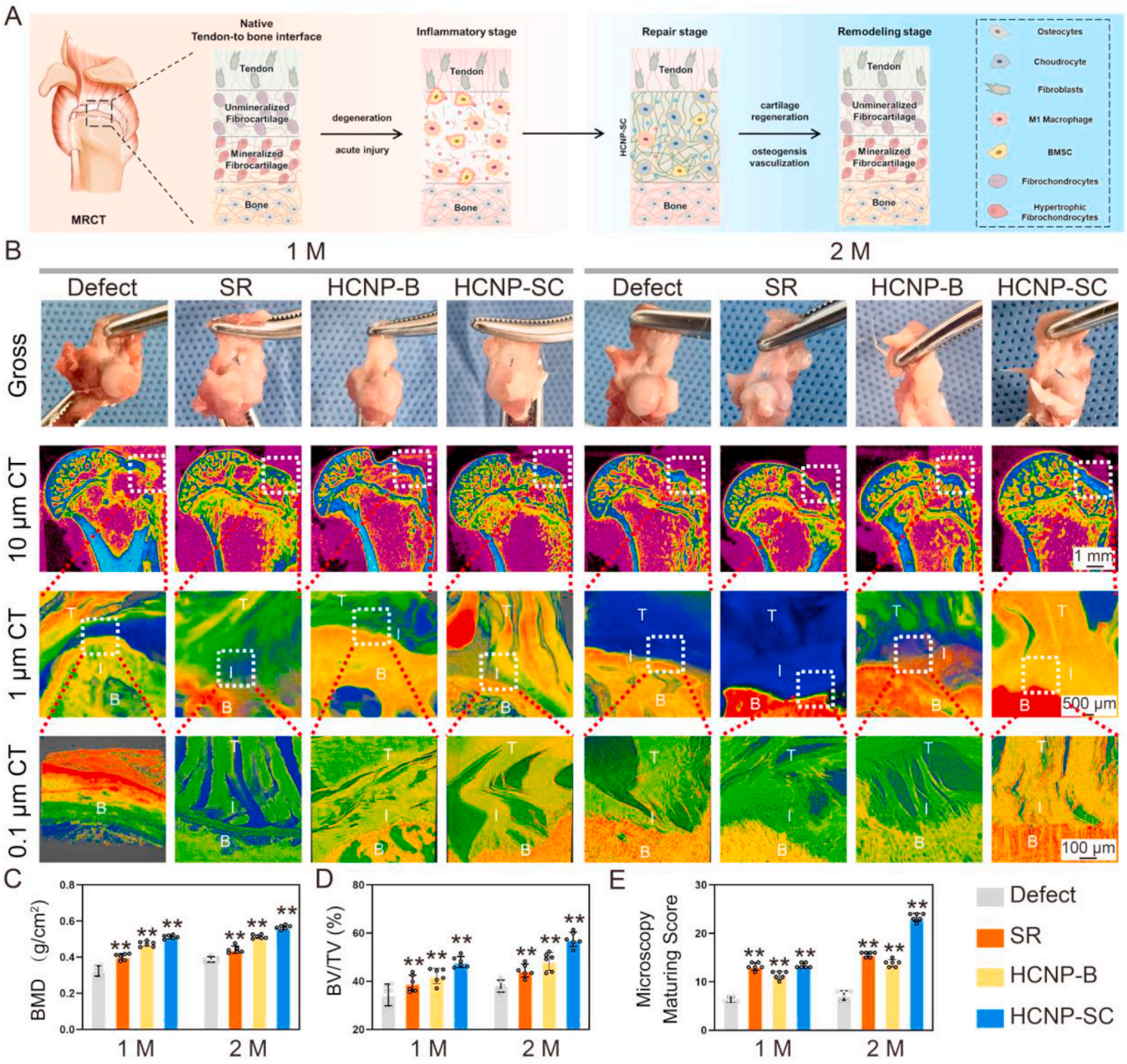

Fig. 4. HCNP promotes microstructural healing at the tendon-to-bone interface. (A) Schematic diagram of tendon-bone interface regeneration. (B) Observation of the tendon-to-bone interface from gross observation to microscopic structure in in the defect, SR, HCNP–B, and HCNP-SC groups at 1 and 2 months postoperatively. Evaluation of subchondral bone changes (C–D) and microscopy maturing score (E) between each group. Significant difference compared with the defect group (**), $P < 0.01$.

1 μm resolution, only discontinuous scar tissue was observed in the rotator cuff footprint area of the defect and SR groups. Fibrous tissue connected to cortical bone was visible in HCNP–B and HCNP-SC groups, but the fiber signal in HCNP–B was weaker, suggesting immature fiber connections. At 0.1 μm resolution, irregular and unoriented fibrous tissue at the interface was noted in the defect, SR, and HCNP–B groups, failing in mechanical transmission. A continuous structure was formed at the tendon-to-bone interface in the HCNP-SC group, characterized as a thick fiber–thin fiber–bone interface. The microscopic histological score of the defect group two months post-surgery was 7.17 ± 0.98, significantly lower than that of the SR group (15.67 ± 0.52), HCNP–B group (13.83 ± 0.75), and HCNP-SC group (23.33 ± 0.82).

3.5. HCNP-SC promotes the restoration of tendon-to-bone interface

In rat models, one month after tendon-to-bone interface repair, hematoxylin-eosin (HE) and Safranin O/Fast green staining showed that the defect group only formed irregular fibers at the tendon-to-bone interface, with no tight tissue connection (Fig. 5A–C). The macroscopic histological score of the defect group was significantly lower at 7.67 ± 0.52, compared to the SR group (18.00 ± 0.63), HCNP–B group (17.33 ± 0.52), and HCNP-SC group (23.17 ± 0.75). In the HCNP–B group, HE and SO/Fast green revealed continuous healing at the tendon-to-bone interface, although the newly formed tissue was disorganized and lacked regular orientation. Conversely, the HCNP-SC group demonstrated effective healing at the tendon-to-bone interface, with noticeable cartilage regeneration. Biomechanical strength one month

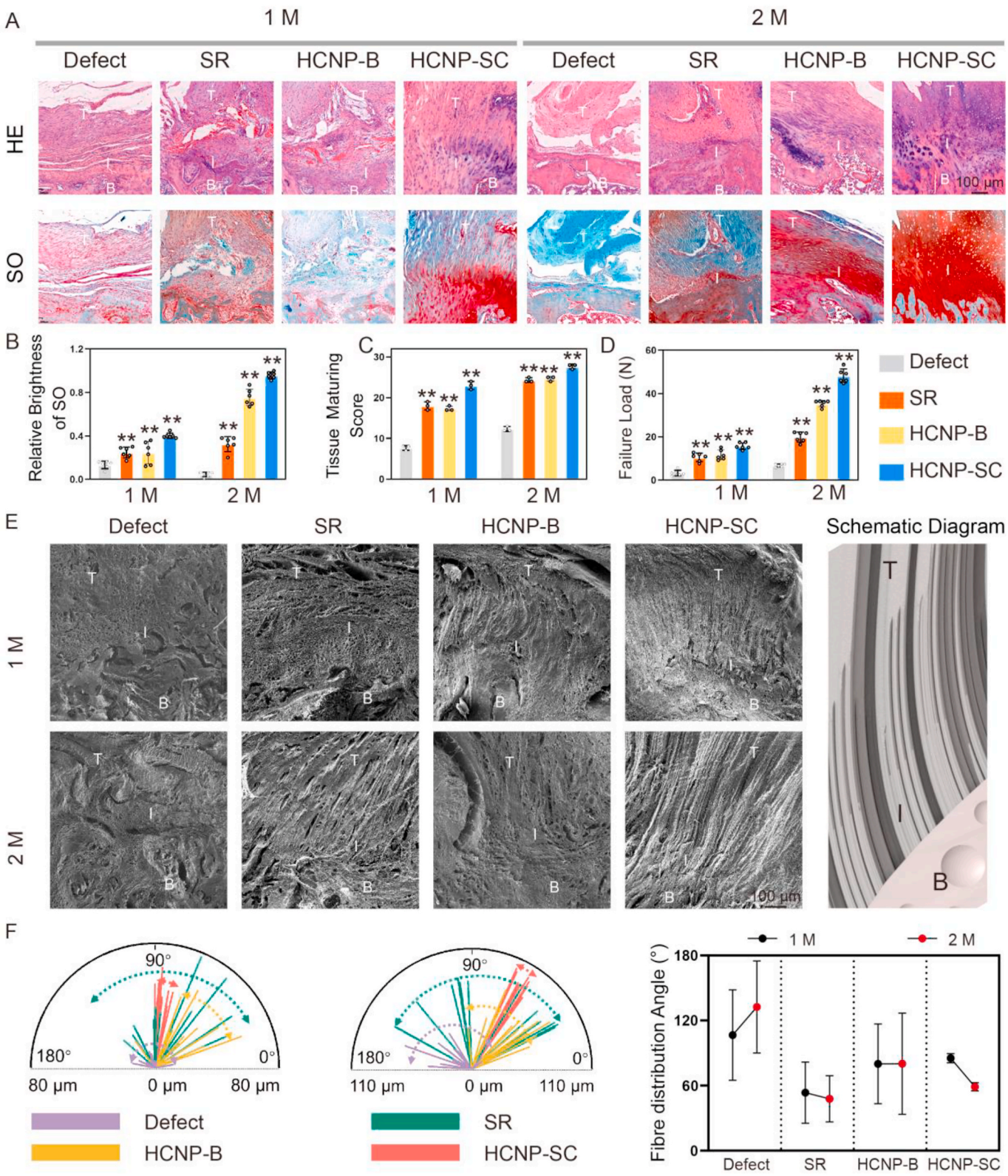

Fig. 5. HCNP promotes the restoration of tri-tissue distribution at the tendon-to-bone interface. Representative images (A) and semi-quantitative (B – C) of the tendon-to-bone interface (HE staining and Safranin O/Fast green staining) in the defect, SR, HCNP–B, and HCNP-SC groups at 1 and 2 months postoperatively. (D) Biomechanical testing of the tendon-to-bone interface. Representative SEM images (E) and fiber orientation analysis (F) of the tendon-bone interface in the four groups at 1 and 2 months postoperatively. SO/Fast green: Safranin O/Fast green; SR: surgical repair; HCNP–B: hierarchical composite nanofiber patch prepared via blending, and HCNP-SC: hierarchical composite nanofiber patch prepared via skeletal copolymerization. **, $P < 0.01$ compared with the defect group, indicating a significant difference.

post-surgery (Fig. 5D) was significantly higher in the SR group (10.52 ± 1.95 N), HCNP–B group (11.67 ± 2.30 N), and HCNP-SC group (15.70 ± 1.53 N) compared to the defect group (3.24 ± 1.29 N). Scanning electron microscopy (SEM) results (Fig. 5E and F) showed that the angle distribution of tendon-to-bone interface fibers ranged from 9.93° to 168.69°, 19.90°–126.47°, 23.69°–138.65°, and 76.66°–90.00° in the defect, SR, HCNP–B, and HCNP-SC groups, respectively, after one month.

Two months post-surgery, more fibrous tissue was observed at the tendon-to-bone interface in the defect group, but the connection between these tissues and the tendon-bone interface remained loose. In the SR group, there was healing between the residual tendon and bone tissue, but with limited cartilage tissue. The macroscopic histological score of the defect group (11.67 ± 1.03) was significantly lower than that of the SR (24.00 ± 0.89), HCNP–B group (24.50 ± 0.84), and HCNP-SC groups (27.67 ± 0.52) after two months. In the HCNP–B group, HE and SO/Fast green staining showed some regenerated cartilage tissue at the tendon-to-bone interface, but in small amounts. In the HCNP-SC group, a substantial amount of regenerated cartilage was observed at the tendon-bone interface on HE and SO/Fast green staining. Biomechanical strength at two months post-surgery was significantly higher in the SR group (19.86 ± 2.34 N), HCNP–B group (35.42 ± 1.47 N), and HCNP-SC group (48.20 ± 3.22 N) compared to the defect group (6.75 ± 0.70 N). SEM revealed that the angle distribution of tendon-to-bone interface fibers was 36.87–176.27°, 21.11–95.19°, 26.57–151.19°, and 54.65–65.96°, respectively, in the defect, SR, HCNP–B, and HCNP-SC groups, indicating that the HCNP-SC can effectively induce directional regeneration at the tendon-bone interface.

3.6. HCNP-SC promotes the restoration of tri-tissue distribution at the tendon-to-bone interface and inhibits inflammatory infiltration in tendon tissue

To further validate the mechanism by which the patch induces regeneration at the tendon-to-bone interface, we performed staining for collagen I, collagen II, and CD206, along with DAPI staining (Fig. 6A). One month post-surgery, immunofluorescence staining for collagen II and CD206 was low at the tendon-to-bone interface of the defect and SR groups. Additionally, the defect group exhibited weaker collagen I staining compared to the SR group. In the HCNP-SC group, CD206 staining was significantly increased, and a notable increase in collagen II staining was also observed. At two months post-surgery, staining for collagen II and CD206 remained low in the tendon-to-bone interface of the defect and SR groups. However, collagen I staining in the SR group was even lower in the second month than in the first month, which may be related to a sustained inflammatory reaction at the tendon-to-bone interface after tendon repair. In the HCNP–B group, a significant increase in collagen I and CD206 expression was observed at the tendon-to-bone interface, although collagen II staining levels were not high. In the HCNP-SC group, staining for CD206, collagen II, and collagen I was significantly high. Since the extracellular matrix (ECM) of tendons, cartilage, and bone tissues is primarily composed of collagen I, II, and I, respectively, the increase in staining of these markers indicates restoration of the tendon-to-bone interface. To further evaluate collagen regeneration at the tendon-to-bone interface, we analyzed the distribution of collagen intensity and localization (Fig. S16). A significant negative correlation between type I and collagen II distribution was observed only in the HCNP-SC group. This three-phase distribution of collagen composition corresponds to the natural histological distribution of bone-cartilage-tendon at the tendon-to-bone interface, indicating that the HCNP-SC can effectively restore the physiological structure of the tendon-to-bone interface.

To verify the scaffold's inhibitory effect on tendon inflammation, we evaluated inflammatory infiltration (Fig. 6B) and collagen distribution analysis (Fig. S17) within the residual tendon tissue. One month after establishing the RCT model, the defect group showed significant infiltration of M1 macrophages expressing iNOS, and collagen I expression in the tendon tissue was significantly decreased. The orientation and cross-sectional area of injured tendon fibers were significantly disrupted (Fig. 6C and Fig. S18). Sirius Red staining of the defect group under polarized light microscopy indicated that the tendon-bone interface was primarily filled with scar tissue composed mainly of type III collagen (Fig. S19). One month post-surgery, RT-qPCR results of tissue samples indicated that the defect group (Col1: 0.64 ± 0.45; Scx: 1.04 ± 0.14; iNOS: 0.97 ± 0.15) had the lowest expression of tendon-related genes and the highest expression of the inflammatory gene compared to the SR group (Col1: 22.26 ± 5.59; Scx: 3.67 ± 0.40; iNOS: 0.49 ± 0.12), HCNP–B group (Col1: 3.40 ± 2.01; Scx: 1.97 ± 0.26; iNOS: 0.31 ± 0.02), and HCNP-SC group (Col1: 8.54 ± 2.03; Scx: 12.86 ± 1.48; iNOS: 0.15 ± 0.05). In the SR group, immunofluorescence staining revealed the presence of M1 macrophage infiltration in the tendon. However, compared to the defect group, the degree of tendon fiber disorientation was lower, and the cross-sectional area was significantly larger. Polarized light microscopy indicated that the residual tendon contains a higher amount of type I collagen. The favorable tendon alignment seen in the SR group at one month is expected, as the tendon tissue is directly affixed to the footprint of the rotator cuff without undergoing a transformational process. In the regenerative tissue of the HCNP–B and HCNP-SC groups, the expression of M1 macrophages was significantly lower than in the defect and SR groups. However, staining for collagen I in the HCNP–B and HCNP-SC groups was lower than in the SR group, as the residual tendon tissue itself contains a large amount of collagen I, and the tendon tissue in the HCNP–B and HCNP-SC groups would need to undergo a regeneration process. Two months after RCT, a continuous infiltration of M1 macrophages and a continued decrease in collagen I expression were observed in the residual tendon tissue. At the same time, the SR group showed a certain decrease in collagen I staining, which may be related to the inability of residual tendon tissue to inhibit M1 macrophage infiltration. In the HCNP–B and HCNP-SC groups, the number of M1 macrophages decreased significantly. However, compared with the HCNP–B group, the HCNP-SC group showed significantly better collagen I staining. RT-qPCR results indicates that the HCNP-SC group (Col1: 12.87 ± 1.48; Scx: 23.65 ± 3.83; iNOS: 0.0018 ± 0.0011) exhibited the highest expression of tendon-related genes and the lowest expression of the inflammatory gene, followed by the SR group (Col1: 6.37 ± 0.94; Scx: 7.50 ± 1.48; iNOS: 0.88 ± 0.02) and the HCNP–B group (Col1: 3.16 ± 0.54; Scx: 2.56 ± 0.62; iNOS: 0.46 ± 0.12), compared to the defect group (Col1: 1.33 ± 0.54; Scx: 1.16 ± 0.28; iNOS: 1.03 ± 0.07). These results suggest that the persistent anti-inflammatory effects of the regenerative patches are also essential for tissue regeneration at the tendon site.

4. Discussion

In this study, we incorporated ferulic acid (FA) into the repeating units of polyurethane through backbone copolymerization, creating a degradable polymer capable of maintaining a persistent anti-inflammatory microenvironment as the polymer degrades. The synthesized poly(ester-ferulic acid-urethane)urea (PEFUU) exhibited notable mechanical properties and processability. We then fabricated a composite patch, named hierarchical composite nanofiber patch (HCNP), using a combination of random and aligned electrospinning. In a rat model of rotator cuff tear (RCT) repair, this patch could partially induce a tri-tissue distribution of bone–cartilage–tendon at the tendon-to-bone interface, promote recovery of continuity and orientation in the micro-connective region between the tendon and cartilage layers, and maintain an anti-inflammatory effect on the residual tendon. The development of HCNP offers a reliable alternative for customizing biological activity in tissue engineering patches.

After tendon-to-bone interface injury, both the residual tendon tissue and the interface experience inflammation, which can lead to the degeneration of type I and collagen II [32,33]. As observed in the SR

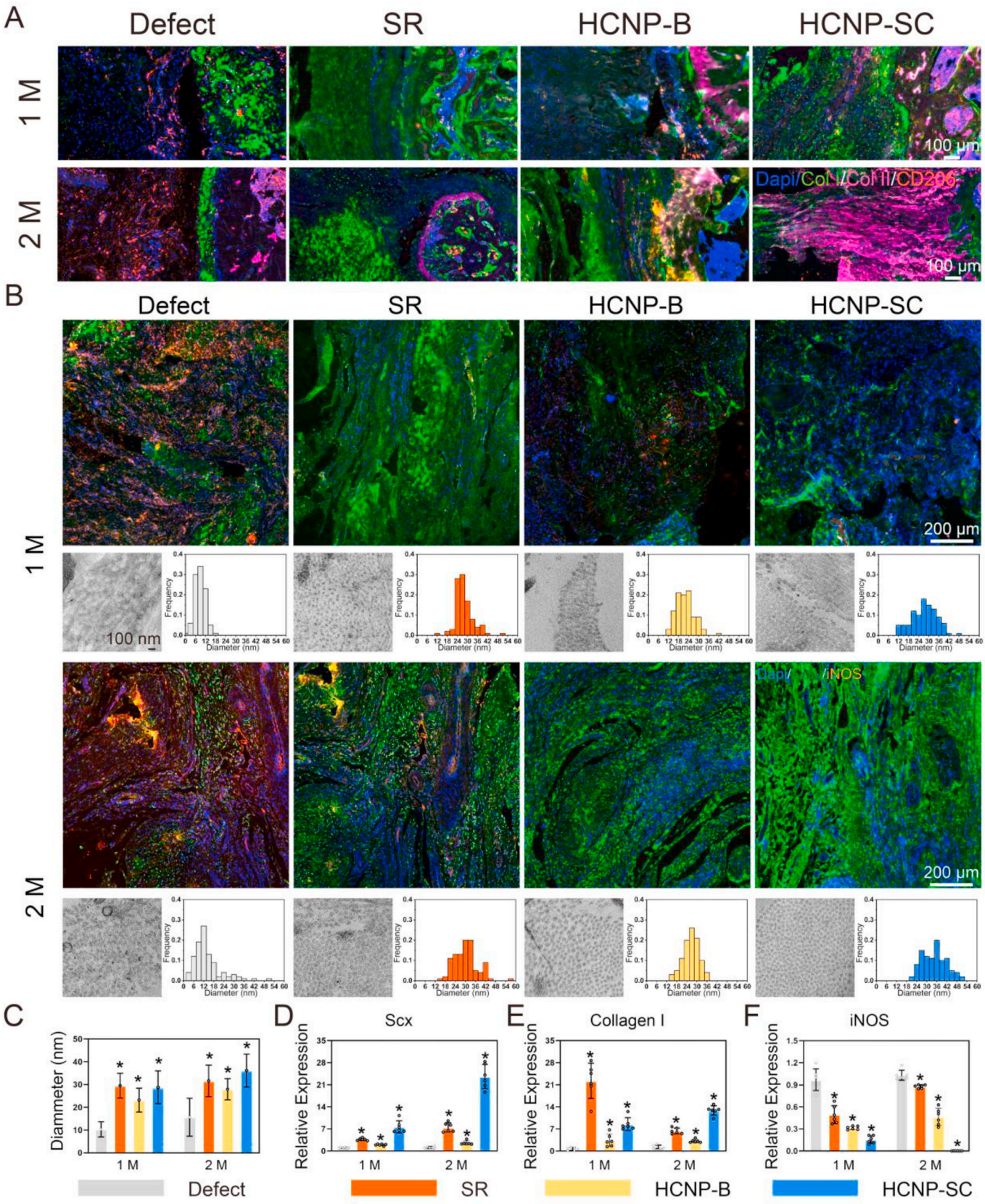

Fig. 6. HCNP-SC inhibits inflammatory infiltration in tendon-to-bone and remnant tendon tissue. (A) Representative immunofluorescence staining images of the tendon-to-bone interfaces in the defect, SR, HCNP–B, and HCNP-SC groups at 1- and 2-months post-surgery (blue: DAPI; green: collagen I; purple: collagen II; yellow: CD206). (B) Representative images and analysis of immunofluorescence and TEM in tendon tissue in the defect, SR, HCNP–B, and HCNP-SC groups at 1 and 2 months postoperatively; (C) Analysis of the diameter of regenerative tendon tissue in the four groups at 1 and 2 months postoperatively. Relative expression levels of (D) Scx, (E) collagen I, and (F) iNOS in the tendon tissue in the four groups at 1 and 2 months postoperatively. **P < 0.01 compared with the defect group, indicating significant differences.

group in this study, without external intervention, the reconstructed RC tissue will continue to exhibit inflammatory infiltration, potentially leading to another tendon tear [34–36]. Therefore, many studies have employed anti-inflammatory drugs to promote RC regeneration [37]. However, current methods can only provide anti-inflammatory effects in the early stages, although the repair of the tendon-to-bone interface is a chronic process. Therefore, the sustained release of anti-inflammatory drugs remains a focus of research in this area. In this study, we synthesized a novel PEFUU that can continuously release the anti-inflammatory drug FA as the patch degrades. Compared with methods that increase the release of anti-inflammatory drugs through slow-release particles, this skeletally copolymerized material showed better processability. Wang et al. used an anti-inflammatory nanofiber membrane to promote scarless tendon regeneration without the need for special processing techniques [38]. However, for injuries in the mechanical transition zone of the tendon-to-bone interface, a single scaffold structure cannot induce optimal healing. The results of the present study demonstrate the processability and drug release characteristics of HCNP, providing a potential reference for subsequent research on drug-based treatment of complex structures in vivo.

Decellularized Wharton's Jelly Tissue (DWJT) is widely utilized in tissue engineering for regeneration due to its abundance of bioactive components, such as hyaluronic acid, and CD31 expression, making it effective in recruiting stem cells [39]. Gao et al. and Yuan et al. employed DWJT for the regeneration of tracheal cartilage and rotator cuff (RC) tissue, respectively, and reported some regenerative effects [40,41]. However, DWJT's processability is limited, and the microstructure of the regenerative induction patch based on DWJT is constrained by its natural structure, which can be simulated or personalized according to the damaged tissue itself. Additionally, due to decellularization, DWJT's mechanical properties are weaker than those of umbilical cord tissue, increasing the risk of patch fracture during regenerative induction [42,43]. Therefore, in this study, hydrolyzed decellularized Wharton's Jelly Tissue (HDWJT) was loaded onto an artificial polymer via freeze-drying to enhance the processability and mechanical properties of the artificial patch, thereby improving the responsiveness of bone marrow mesenchymal stem cells (BMSCs) to the patch microstructure and making the constructed composite material more suitable for in vivo regenerative induction.

The tendon-to-bone interface serves as a mechanical connection between bone and tendon, two tissues with vastly different mechanical properties [44]. Typically, the connection between materials with significantly different mechanical properties is the weakest part of the structure [45]. However, biomechanical experiments on the normal tendon-to-bone interface have shown that fractures occur at the site of the tendon or bone and rarely at the tendon-to-bone interface, indicating that the mechanical strength of the tendon-to-bone interface exceeds that of both tendon and bone tissue. Rossetti et al. highlighted that the great mechanical strength of the tendon-bone interface can be attributed to the dispersed structure of tendon fibers, from thick fibers to thin fibers, with the main load-bearing structure being the thin fibers composed mainly of collagen II [46]. However, simple surgical repair can only restore the continuity of collagen I and cannot restore collagen II at the tendon-to-bone interface. Previous studies on RC repair have often focused on cartilage regeneration at the tendon-to-bone interface, without examining the distribution of type I-II-I collagen at the interface [47]. Our previous research indicates that the restoration of this three-phase distribution may be crucial for the restoration of the tendon–bone structure. Additionally, conventional imaging methods for the tendon-to-bone interface, such as micro-CT, only allow us to evaluate the degeneration of bone tissue in the footprint area of the tendon tissue and to speculate about the actual regeneration at the tendon-to-bone interface [48,49]. To our knowledge, the present study is the first to observe the complete process of tissue regeneration in various treatment groups using X-ray microscopy (XRM). The findings revealed that the failure of simple surgical repair is not only due to inflammatory infiltration causing tendon degeneration but is also related to the challenges of integrating autogenous tendons with bone tissue. The biologically active HCNP constructed in this study can effectively induce the formation of a thick–thin fiber-connected microstructure at the tendon-to-bone interface, thereby increasing the overall mechanical strength of the tendon-bone interface.

The development of biomimetic scaffolds is a prominent and innovative area in tissue engineering scaffold research in recent years. Given the unique structure of the tendon-bone interface, constructing a scaffold that replicates the natural structure of the tendon-bone interface could be more advantageous for tissue regeneration. Bianchi et al. constructed disordered and oriented layers of rotator cuff patches by controlling the speed of a cylindrical inox-steel rotating drum and incorporated nanohydroxyapatite in the disordered layer to enhance the regeneration of subchondral bone [50]. Orr et al. manipulated the morphology of nanofibers using a magnetic field, resulting in a relatively oriented nanostructure at the initial assembly [51]. Xie et al. applied an electric field at the collection of nanofibers, also creating disordered and oriented layers of biomimetic rotator cuff natural structures [52]. In our study, we adopted a similar construction method to that of Bianchi et al., which is more convenient as it involves regulating the drum speed to construct the biomimetic rotator cuff scaffold. This method aligns with our strategy of constructing PEFUU through skeletal copolymerization of ferulic acid, avoiding repeated medication during use and future complex reviews of drug-device combinations. We will further explore the possibility of constructing rotator cuff patches using pre-applied magnetic fields or electric fields in future experiments, providing additional insights for the development of rotator cuff patches.

There are several limitations in this study. First, our rat rotator cuff repair model demonstrated an enhanced regenerative response, partly due to the inherently strong regenerative capabilities of rodent tissues. While the excessive chondrogenesis observed in our model might be considered pathogenic in a clinical context, such outcomes in animal models can offer valuable insights. Second, this study lacks mechanical performance testing of the HCNP after implantation to assess its structural integrity and stability. However, after 1 and 2 months post-implantation, the scaffolds are often enveloped by synovial tissue, and due to their small size (considering the small anatomy of the rat rotator cuff), it becomes challenging to extract them for subsequent mechanical testing. Third, our research on macrophage subtypes in this study remained at the relatively basic level of M1 and M2 types. While these are the primary focus for most immunomodulatory material studies, future research should delve deeper into how PEFUU regulates the functional subtypes of M1 and M2 macrophages. Fourthly, this study lacks a comprehensive understanding of the immunomodulatory ability of HCNP-SC within the first 7–14 days of implantation. As the immune response is known to play a crucial role in the early stages of damage repair, focusing more on the immune response within this time frame could provide valuable insights into the initial interactions between the scaffold and the host tissue. Future studies will aim to address this gap by investigating the immunomodulatory effects of HCNP-SC during the critical early phase of tissue repair.

Overall, in this study, we designed and synthesized a novel anti-inflammatory polymer, PEFUU, which could maintain a stable FA release rate of around 0.2 μg/day for up to 24 days. We used it to construct an HCNP-SC loaded with HDWJT. This double-layered patch could increase the responsiveness of stem cells to the microstructure of the patch in the early stages, thereby inducing the directional differentiation of stem cells. Additionally, since the patch was copolymerized with effective anti-inflammatory small molecules, it could suppress the secretion of TNF-α (relative ratio from 189.78 ± 41.02 to 24.40 ± 11.12) and promote the secretion of IL-10 (relative ratio from 0.86 ± 0.25 to 3.28 ± 0.62) from macrophages. Thus, as the patch degraded, it altered the inflammatory niche after RCT, inducing a promising anti-inflammatory effect throughout the regeneration process. After 2 months of implantation in rats, the double-layered PEFUU-WJ patch

effectively induced microstructural regeneration at the tendon-to-bone interface and restored the physiological distribution of type I-II-I collagen at the tendon-bone interface (Pearson correlation coefficient = −0.525, $P < 0.05$). This study provides an idea for the use of an electrospun nanofiber mat in tissue regeneration. By introducing anti-inflammatory small molecules through copolymerization, the inflammatory niche of the damaged tissue can be persistently altered, effectively inducing tissue regeneration.

Funding

The 74nd Postdoctoral Science Foundation of China 2024M362720 (L. W.).

Regenerative Sports Medicine and Translational Youth Science and Technology Innovation Workroom (J. Z.).

Technology Support Project of Science and Technology Commission of Shanghai Municipality 21S31908500 (J. Z.).

CRediT authorship contribution statement

Liren Wang: Funding acquisition, Validation, Visualization, Writing – original draft. **Yonghang Liu:** Validation, Methodology, Investigation, Formal analysis, Data curation, Conceptualization, Visualization, Writing – original draft, Writing – review & editing. **Zhiqi Lin:** Yuhao Kang: Project administration, Validation, Visualization. **Huiang Chen:** Resources, Software, Supervision. **Bowen Liu:** Investigation, Methodology. **Xiaoyu Yan:** Funding acquisition, Investigation. **Tonghe Zhu:** Conceptualization, Data curation, Formal analysis, Funding acquisition. **Qin Zhang:** Funding acquisition, Supervision, Validation. **Jinzhong Zhao:** Supervision, Validation, **Haihan Gao:** Data curation, Formal analysis. **Haocheng Jin:** Investigation, Methodology, Project administration.

Acknowledgements

Liren Wang and Yonghang Liu contributed equally to this work.

Appendix A. Supplementary data

Supplementary data to this article can be found online at https://doi.org/10.1016/j.bioactmat.2024.03.029.

References

[1] A. Yamamoto, K. Takagishi, T. Osawa, et al., Prevalence and risk factors of a rotator cuff tear in the general population, J. Shoulder Elbow Surg. 19 (1) (2010) 116–120.
[2] G.M. Genin, S. Thomopoulos, The tendon-to-bone attachment: Unification through disarray, Nat. Mater. 16 (6) (2017) 607–608.
[3] L. Wang, J. Jiang, H. Lin, et al., Advances in regenerative Sports medicine research, Front. Bioeng. Biotechnol. 10 (2022) 908751.
[4] G. Nourissat, F. Berenbaum, D. Duprez, Tendon injury: from biology to tendon repair, Nat. Rev. Rheumatol. 11 (4) (2015) 223–233.
[5] F. Fang, A.G. Schwartz, E.R. Moore, et al., Primary cilia as the nexus of biophysical and hedgehog signaling at the tendon enthesis, Sci. Adv. 6 (44) (2020).
[6] J. Liu, S. Lin, X. Liu, et al., Fatigue-resistant adhesion of hydrogels, Nat. Commun. 11 (1) (2020) 1071.
[7] L. Du, C. Qin, H. Zhang, et al., Multicellular Bioprinting of biomimetic Inks for tendon-to-bone regeneration, Adv. Sci. 10 (21) (2023) e2301309.
[8] R.J. Murphy, K. Kliskey, K. Wheway, et al., Rotator cuff tendinopathy: immunohistochemical changes across the spectrum of pathology, Int. J. Exp. Pathol. 94 (4) (2013) A9–A.
[9] A. Batsivari, M.L.R. Haltalli, D. Passaro, et al., Dynamic responses of the haematopoietic stem cell niche to diverse stresses, Nat. Cell Biol. 22 (1) (2020) 7–17.
[10] C.S. Morrow, D.L. Moore, Stem cell aging? Blame it on the niche, Cell Stem Cell 24 (3) (2019) 353–354.
[11] C. Zhao, J. Chen, J. Ye, et al., Structural transformative antioxidants for Dual-Responsive anti-inflammatory delivery and Photoacoustic inflammation imaging, Angew Chem. Int. Ed. Engl. 60 (26) (2021) 14458–14466.
[12] B. Yang, B. Zhou, C. Li, et al., A Biostable l-DNA hydrogel with improved stability for Biomedical applications, Angew Chem. Int. Ed. Engl. 61 (30) (2022) e202202520.
[13] C.S. Proctor, Long-term successful arthroscopic repair of large and massive rotator cuff tears with a functional and degradable reinforcement device, J. Shoulder Elbow Surg. 23 (10) (2014) 1508–1513.
[14] B.A. Lenart, K.A. Martens, K.A. Kearns, et al., Treatment of massive and recurrent rotator cuff tears augmented with a poly-l-lactide graft, a preliminary study, J. Shoulder Elbow Surg. 24 (6) (2015) 915–921.
[15] C.S. Shin, F.J. Cabrera, R. Lee, et al., 3D-Bioprinted inflammation modulating polymer scaffolds for soft tissue repair, Adv Mater 33 (4) (2021) e2003778.
[16] J. Wu, Y. Yu, Y. Cheng, et al., Ligand-dependent activity engineering of Glutathione Peroxidase-mimicking MIL-47(V) Metal-Organic Framework Nanozyme for Therapy, Angew Chem. Int. Ed. Engl. 60 (3) (2021) 1227–1234.
[17] M.H. Bai, B.S. Zhao, Z.Y.T. Liu, et al., Mucosa-like Conformal hydrogel coating for Aqueous Lubrication, Adv. Mater. 34 (46) (2022).
[18] Y. Chen, P. Gao, L. Huang, et al., A tough nitric oxide-eluting hydrogel coating suppresses neointimal hyperplasia on vascular stent, Nat. Commun. 12 (1) (2021).
[19] L. Wang, Y. Kang, Y. Wei, et al., Rotator cuff tear reaching the superior half portion of the humeral head causes shoulder abduction malfunction, Knee Surg. Sports Traumatol. Arthrosc. (2022).
[20] S. Talebian, B. Mendes, J. Conniot, et al., Biopolymeric coatings for local release of therapeutics from Biomedical Implants, Adv. Sci. (2023) e2207603.
[21] W. Ma, Z. Liu, T.H. Zhu, et al., Fabric-enhanced vascular graft with hierarchical structure for promoting the regeneration of vascular tissue, Adv. Healthcare Mater. (2024) e2302676.
[22] B. Chen, Y. Liang, J. Zhang, et al., Synergistic enhancement of tendon-to-bone healing via anti-inflammatory and pro-differentiation effects caused by sustained release of Mg(2+)/curcumin from injectable self-healing hydrogels, Theranostics 11 (12) (2021) 5911–5925.
[23] J. Ide, T. Tokunaga, Rotator cuff tendon-to-bone healing at 12 months after patch grafting of acellular dermal matrix in an animal model, J. Orthop. Sci. 23 (2) (2018) 207–212.
[24] D.H. Kim, S.G. Min, J.P. Yoon, et al., Mechanical Augmentation with absorbable Alginate Sheet enhances healing of the rotator cuff, Orthopedics 42 (1) (2019) e104–e110.
[25] C.G. Zalavras, R. Gardocki, E. Huang, et al., Reconstruction of large rotator cuff tendon defects with porcine small intestinal submucosa in an animal model, J. Shoulder Elbow Surg. 15 (2) (2006) 224–231.
[26] Y. H. Liu, L. R. Wang, Z. Liu, et al., Durable immunomodulatory nanofiber niche for the functional remodeling of cardiovascular tissue, ACS Nano 18 (1) 951–971.
[27] K.H.J. West, C.G. Gahan, P.R. Kierski, et al., Sustained release of a Synthetic Autoinducing Peptide Mimetic Blocks Bacterial Communication and Virulence in vivo, Angew Chem. Int. Ed. Engl. 61 (24) (2022) e202201798.
[28] J. Park, J.S. Zeng, A. Sahasrabudhe, et al., Electrochemical modulation of Carbon Monoxide-Mediated cell signaling, Angew Chem. Int. Ed. Engl. 60 (37) (2021) 20325–20330.
[29] G.F. Del Castillo, M. Kyriakidou, Z. Adali, et al., Electrically Switchable polymer Brushes for protein Capture and release in biological environments, Angew Chem. Int. Ed. Engl. 61 (22) (2022) e202115745.
[30] L. Rossetti, L.A. Kuntz, E. Kunold, et al., The microstructure and micromechanics of the tendon-bone insertion, Nat. Mater. 16 (6) (2017) 664–670.
[31] A. Daghrery, J.A. Ferreira, J. Xu, et al., Tissue-specific melt electrowritten polymeric scaffolds for coordinated regeneration of soft and hard periodontal tissues, Bioact. Mater. 19 (2023) 268–281.
[32] J.P. Sherlock, B. Joyce-Shaikh, S.P. Turner, et al., IL-23 induces spondyloarthropathy by acting on ROR-gammat+ CD3+CD4-CD8- entheseal resident T cells, Nat Med 18 (7) (2012) 1069–1076.
[33] C. Lehner, G. Spitzer, P. Langthaler, et al., Allergy-induced systemic inflammation impairs tendon quality, EBioMedicine 75 (2022) 103778.
[34] Y. Chen, F. Jiang, H. Li, et al., Retears and Concomitant functional Impairments after rotator cuff repair: shoulder activity as a risk factor, Am. J. Sports Med. 48 (4) (2020) 931–938.
[35] P. Lapner, M. Bouliane, J.W. Pollock, et al., Intraoperative Channeling in arthroscopic rotator cuff repair: a Multicenter Randomized controlled trial, Am. J. Sports Med. 51 (2) (2023) 323–330.
[36] G. Kim, S. Kim, Y. Lee, et al., Prognostic factors leading to good or poor outcomes based on functional and radiological findings after a rotator cuff retear, Am J Sport Med (2022).
[37] H.H. Gao, L.R. Wang, H.C. Jin, et al., Regulating macrophages through immunomodulatory biomaterials is a promising strategy for promoting tendon-bone healing, J. Funct. Biomater. 13 (4) (2022).
[38] Z. Wang, L. Xiang, F. Lin, et al., A biomaterial-based Hedging immune strategy for scarless tendon healing, Adv. Mater. 34 (19) (2022).
[39] Y. Xu, H. Duan, Y.Q. Li, et al., Nanofibrillar decellularized Wharton's jelly matrix for segmental tracheal repair, Adv. Funct. Mater. 30 (14) (2020).
[40] E.R. Gao, Y. Wang, P.L. Wang, et al., C-shaped cartilage development using Wharton's jelly-derived hydrogels to Assemble a highly biomimetic Neotrachea for use in Circumferential tracheal reconstruction, Adv. Funct. Mater. (2023).
[41] Z.G. Yuan, H. Li, S.L. He, et al., Kartogenin releasing decellularized umbilical cord Wharton's jelly scaffold promotes rotator cuff fibrocartilaginous interface regeneration, Mater. Des. 218 (2022).
[42] M.K. Kim, W. Jeong, S.M. Lee, et al., Decellularized extracellular matrix-based bio-ink with enhanced 3D printability and mechanical properties, Biofabrication 12 (2) (2020).
[43] A.T. Pereira, K.H. Schneider, P.C. Henriques, et al., Graphene oxide coating improves the mechanical and biological properties of decellularized umbilical cord Arteries, Acs Appl Mater Inter 13 (28) (2021) 32662–32672.

[44] S. Choi, J.R. Moon, N. Park, et al., Bone-adhesive Anisotropic tough hydrogel mimicking tendon enthesis, Adv. Mater. (2022).
[45] R.A.S.H. Chang, J.F. Shanley, M.E. Kersh, et al., Tough and tunable scaffold-hydrogel composite biomaterial for soft-to-hard musculoskeletal tissue interfaces, Sci. Adv. 6 (34) (2020).
[46] L. Rossetti, L.A. Kuntz, E. Kunold, et al., The microstructure and micromechanics of the tendon-bone insertion, Nat. Mater. 16 (6) (2017) 664.
[47] L.R. Wang, T.H. Zhu, Y.H. Kang, et al., Crimped nanofiber scaffold mimicking tendon-to-bone interface for fatty-infiltrated massive rotator cuff repair, Bioact. Mater. 16 (2022) 149–161.
[48] R.H. Yang, G. Li, C.Y. Zhuang, et al., Gradient bimetallic ion-based hydrogels for tissue microstructure reconstruction of tendon-to-bone insertion, Sci. Adv. 7 (26) (2021).
[49] R.H. Yang, Y.L. Zheng, Y. Zhang, et al., Bipolar metal Flexible electrospun fibrous membrane based on Metal-Organic Framework for gradient healing of tendon-to-bone interface regeneration, Adv. Healthcare Mater. 11 (12) (2022).
[50] E. Bianchi, A. Faccendini, E. Del Favero, et al., Topographical and compositional gradient Tubular scaffold for bone to tendon interface regeneration, Pharmaceutics 14 (10) (2022).
[51] S.B. Orr, A. Chainani, K.J. Hippensteel, et al., Aligned multilayered electrospun scaffolds for rotator cuff tendon tissue engineering, Acta Biomater. 24 (2015) 117–126.
[52] J. Xie, X. Li, J. Lipner, et al., "Aligned-to-random" nanofiber scaffolds for mimicking the structure of the tendon-to-bone insertion site, Nanoscale 2 (6) (2010) 923–926.